Geomechanics and Engineering, *Vol. 20, No. 2 (2020) 165-174*
DOI: https://doi.org/10.12989/gae.2020.20.2.165

Stiffness loss in enzyme-induced carbonate precipitated sand with stress scenarios

Jun Young Song[1a], Youngjong Sim[2b], Sun Yeom[3c], Jaewon Jang[4d] and Tae Sup Yun*[5]

[1]Korea Polar Research Institute, Incheon 21990, Republic of Korea
[2]Land and Housing Institute, Korea Land and Housing Corporation, Daejeon 34047, Republic of Korea
[3]Korea Institute of Civil Engineering and Building Technology, Gyeonggi-Do 10223, Republic of Korea
[4]Department of Civil and Environmental Engineering, Hanyang University, Seoul 04763, Republic of Korea
[5]Department of Civil and Environmental Engineering, Yonsei University, Seoul 03722, Republic of Korea

(Received March 19, 2019, Revised November 8, 2019, Accepted January 15, 2020)

Abstract. The enzyme-induced carbonate precipitation (EICP) method has been investigated to improve the hydro-mechanical properties of natural soil deposits. This study was conducted to explore the stiffness evolution during various stress scenarios. First, the optimal concentration of urea, $CaCl_2$, and urease for the maximum efficiency of calcite precipitation was identified. The results show that the optimal recipe is 0.5 g/L and 0.9 g/L of urease for 0.5 M $CaCl_2$ and 1 M $CaCl_2$ solutions with a urea-$CaCl_2$ molar ratio of 1.5. The shear stiffness of EICP-treated sands remains constant up to debonding stresses, and further loading induces the reduction of S-wave velocity. It was also found that the debonding stress at which stiffness loss occurs depends on the void ratio, not on cementation solution. Repeated loading-unloading deteriorates the bonding quality, thereby reducing the debonding stress. Scanning electron microscopy and X-ray images reveal that higher concentrations of $CaCl_2$ solution facilitate heterogeneous nucleation to form larger $CaCO_3$ nodules and 11-12 % of $CaCO_3$ forms at the inter-particle contact as the main contributor to the evolution of shear stiffness.

Keywords: enzyme; $CaCO_3$; debonding; shear stiffness; stress relaxation; X-ray CT

1. Introduction

Natural soils inherently composed of particulate grains are subjected to various weathering and aging processes, which result in a partially or fully cemented state (Fernandez and Santamarina 2001). Because cemented soils are omnipresent in nature and their hydro-mechanical characteristics play a significant role in engineering design, naturally or artificially cemented soils have been extensively studied for decades to examine the evolutionary behaviors and geotechnical properties (Consoli *et al.* 1998, Huang and Airey 1998, Ismail *et al.* 2002, Kaniraj and Havanagi 2001, Rios *et al.* 2014). The cementation process binds soil particles together by cementing agents such as amorphous silica, oxides, hydrous silicates, and calcium carbonate (DeJong *et al.* 2006, O'Rourke and Crespo 1988), which modifies the geotechnical properties such as improved stiffness and strength, as well as liquefaction resistance (Huang and Airey 1998, Saxena *et al.* 1988), and permeability reduction (Bahar *et al.* 2004). Recently, microbial activity has been explored as an artificial cementation or clogging technology for ground improvement (Al Qabany and Soga 2013, Chu *et al.* 2014, Cui *et al.* 2017, DeJong *et al.* 2006, Jiang *et al.* 2017, Kim *et al.* 2017, Lin *et al.* 2016, Mahawish *et al.* 2018, Montoya *et al.* 2013, van Paassen *et al.* 2010, Yasuhara *et al.* 2012). The microbial process involves urea hydrolysis with the help of bacteria (Eq. (1)), and the produced carbonate ion (CO_3^{2-}) reacts with injected calcium ion (Ca^{2+}) yielding calcium carbonate ($CaCO_3$) (Eq. (2)).

$$\mathrm{CO(NH_2)_2 + 2H_2O \xrightarrow[\text{Enzyme}]{\text{Bacteria}} 2NH_4^{\ +} + CO_3^{\ 2-}} \tag{1}$$

$$\mathrm{Ca^{2+} + CO_3^{\ 2-} \rightarrow CaCO_3} \tag{2}$$

This process is called microbial-induced carbonate precipitation (MICP) and is often used because of the omnipresent ureolytic bacteria in the soil (Burbank *et al.* 2012), but sometimes is associated with limitations and difficulties such as $CaCO_3$ precipitation near the bacteria cell wall, resulting in process inactivation due to the limited nutrient and water transfer (Cuthbert *et al.* 2012, De Muynck *et al.* 2010, Mitchell and Santamarina 2005), and the difficult control of the precipitation site and rate that is governed by bacterial distribution and conditions. However, the direct use of enzymes in this application can manipulate and control the targeted performance.

---

*Corresponding author, Professor
E-mail: taesup@yonsei.ac.kr
[a]Overwintering Researcher
E-mail: somg3569@gmail.com
[b]Senior Researcher
E-mail: yjsim@lh.or.kr
[c]Technician
E-mail: duatjs@kict.re.kr
[d]Associate Professor
E-mail: jwj@hanyang.ac.kr

http://www.techno-press.org/?journal=gae&subpage=7
ISSN: 2005-307X (Print), 2092-6219 (Online)

The soils improved by $CaCO_3$ precipitation tend to experience a change in loading conditions such as stress relaxation during soil cutting or additional compressive loading by building structures, which result in stiffness loss or skeletal collapse (Yun and Santamarina 2005). In addition, once the natural soils under various degrees of confining stress and with various relative densities are treated with different degrees of cementation, the treated soils may exhibit unexpected evolution of stiffness upon loading and unloading (Fernandez and Santamarina 2001). Therefore, the evolution of load-resisting behaviors in the treated soils requires in-depth understanding to economically design the appropriate soil improvements and to avoid any potential losses induced by stiffness changes.

This study was conducted to explore how the soils cemented with $CaCO_3$ precipitation behave for various loading sequences and show the pattern of $CaCO_3$ precipitation in pore space. Because the debonding of precipitated $CaCO_3$ is well reflected in the shear stiffness loss, the shear wave velocity is measured in the K_0-condition at each loading stage. Scanning electron microscopy (SEM) imaging and 3D X-ray microcomputed tomographic (μ-CT) imaging of cemented soils help understand the morphological features of precipitated $CaCO_3$ in pore space and its attribution to the stiffness evolution.

2. Experimental study

2.1 Optimal recipe for $CaCO_3$ formation

The amount of produced $CaCO_3$ strongly depends on the molar ratio of urea to $CaCl_2$ and urease concentration; thus, a series of reaction tests with different concentrations of urea, urease, and $CaCl_2$ was systematically performed to determine the optimal recipe of each component: 1) molar ratios of urea to $CaCl_2$ from 1 to 2.5 with 0.25 increment at a constant urease concentration of 0.5 g/L, and 2) urease concentration from 0.1 g/L to 0.9 g/L at 1.5 molar ratio of urea to $CaCl_2$ for 0.5 M and 1 M $CaCl_2$ molar concentration.

Two solutions were separately prepared: one solution including urea (U5378, Sigma Aldrich), $CaCl_2 \cdot 2H_2O$ (C3881, Sigma Aldrich), and NaOH (Duksan); and another solution including only urease (U1500, Sigma Aldrich, Jack Bean urease, 40,150 U/g activity). Note that 1.5×10^{-4} M NaOH was added to the urea and $CaCl_2$ solution to achieve a favorable reaction at pH 8–9. Each solution was thoroughly mixed by a mechanical stirrer (MTOPS, HSD 180) at 300 rpm for 1 min. Then, 7.5 ml of each solution was poured into a 15-ml sterilized conical tube, followed by gentle shaking for 1 min. The reaction was allowed to proceed for 7 days at room temperature (20 ± 1.5 ℃).

Fig. 1 shows the precipitation of $CaCO_3$ in the conical tube with time. The $CaCO_3$ initially appears to be floating and is gradually precipitated to the bottom. There is no noticeable change after 12 h. After 7 days, the supernatant in the tube was removed and the precipitated remainder was dried at 80 °C for 24 h. The mass of produced $CaCO_3$ was measured by the rapid carbonate analyzer specified in ASTM D4373-14, which designates the gas pressure of CO_2 proportional to the mass of $CaCO_3$ when it reacts with HCl.

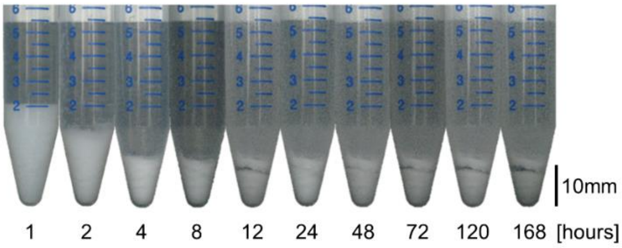

Fig. 1 Precipitation of $CaCO_3$ in a 15 ml sterilized conical tube for 7 days. The $CaCO_3$ is nucleated and settled to the bottom with time

$$CaCO_3 + 2HCl \rightarrow CaCl_2 + CO_2 + H_2O \qquad (3)$$

The theoretically producible maximum mass can be obtained as follows; 1 M $CaCl_2$ is required to produce 1 M $CaCO_3$ (Eq. (4)) and the mass of 1 M $CaCO_3$ in 1 L solution is 100.09 g. Under 100 % reaction efficiency, the mole of precipitated $CaCO_3$ is the same as the mole of the used $CaCl_2$:

$$CaCl_2 \cdot 2H_2O + CO(NH_2)_2 \xrightarrow{\text{urease}} CaCO_3 + 2NH_4Cl \qquad (4)$$

Generally, the mole of precipitated $CaCO_3$ is less than the mole of injected $CaCl_2$; the reaction efficiency is defined as the ratio of the mole of the precipitated $CaCO_3$ to the mole of injected $CaCl_2$.

Three samples were prepared using the same concentrations of urea, $CaCl_2$, and urease, and the reaction efficiency was measured to obtain the optimal ratio of solutions. Fig. 2 shows the average and standard deviation of the three test results. For 0.5 M $CaCl_2$, the reaction efficiency increases from 85 % as the urea-$CaCl_2$ molar ratio increases and reaches 100 % for a urea-$CaCl_2$ ratio over 1.5 (Fig. 2a). Note that the $CaCO_3$ is assumed to be produced at maximum when the molar concentration of urea is 1.5 times that of $CaCl_2$. As the urea-$CaCl_2$ molar ratio increases, the formation efficiency then asymptotically converges to 100% because the reactant (Ca^{2+}) limitedly exists in the solution despite the redundantly decomposed urea. For 1 M $CaCl_2$, the reaction efficiency increases from 65 % to 70 % when the urea-$CaCl_2$ ratio increases from 1 to 1.5. Then, the reaction efficiency gently decreases with further increasing urea-$CaCl_2$ molar ratio. This behavior is attributed to the fact that the urease is composed of a protein whose solubility increases to some extent while the salting-out phenomenon occurs, resulting in the inhibition of urease activity as the urea-$CaCl_2$ molar ratio increases (Hamdan 2015). Nonetheless, it is obvious that the urea-$CaCl_2$ molar ratio of 1.5 seems to yield the maximum amount of $CaCO_3$ regardless of $CaCl_2$ concentration. For the given urea-$CaCl_2$ molar ratio of 1.5, the reaction efficiency sharply increases as the urease concentration increases from 0.1 to 0.3 g/L (Fig. 2b). For 0.5 M $CaCl_2$, 100 % reaction efficiency is achieved at 0.5 g/L of urease concentration and remains constant afterwards. On the other

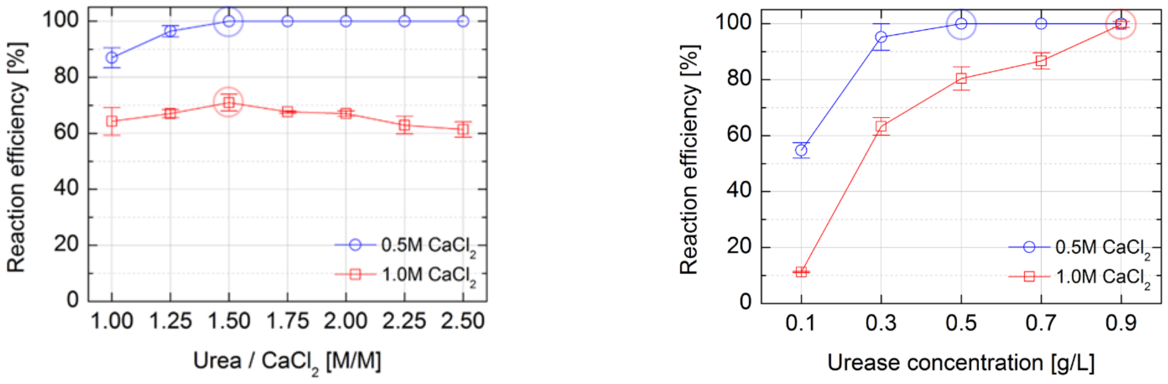

(a) (b)

Fig. 2 Reaction efficiency as a function of (a) urea-$CaCl_2$ ratio and (b) urease concentration for 0.5 M and 1 M $CaCl_2$ solution for urea-$CaCl_2$ ratio of 1

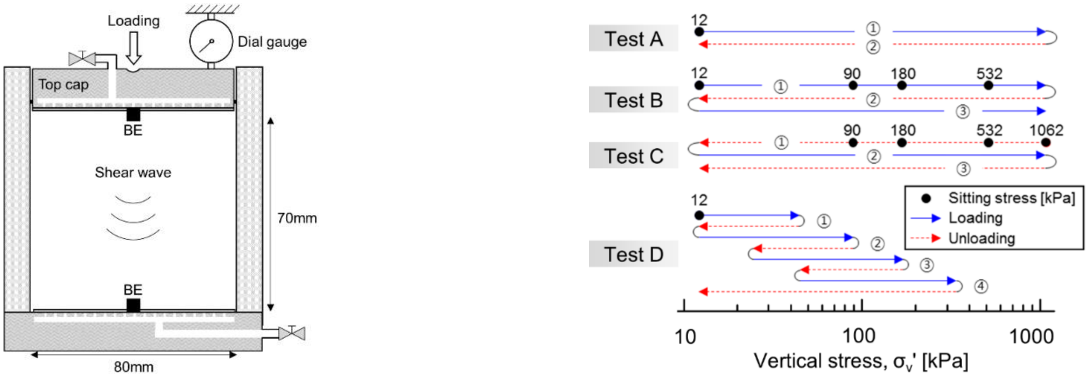

(a) (b)

Fig. 3 (a) Oedometric cell equipped with bender element (BE) for measuring shear wave velocity and (b) Loading sequences for Tests A to D. For test A, samples are made with 0.5 M and 1 M of $CaCl_2$ concentration and 30 % and 70 % of relative density. All other tests are conducted with samples made of 0.5 M $CaCl_2$ and 70 % relative density

hand, for 1 M $CaCl_2$ solution, the reaction efficiency continues to increase to 98 % until the urease concentration reaches 0.9 g/L. In the same manner, the reactant (Ca^{2+}) is limited at 0.5 M $CaCl_2$, whereas the reactant is sufficient to react with CO_3^{2-} at 1 M $CaCl_2$ as the urease concentration increases. From these results, the urea-$CaCl_2$ molar ratio of 1.5 was used, and the urease concentration of 0.5 g/L for 0.5 M $CaCl_2$ and 0.9 g/L for 1 M $CaCl_2$ was used for the rest of the experimental studies.

2.2 Experimental procedures

The diameter of the employed oedometric cell made of polycarbonate was D = 80 mm and the height was H = 70 mm. A pair of bender elements was embedded into the top and bottom caps to measure the shear (S-) wave velocity (Fig. 3a). The S-wave velocity is highly sensitive to the inter-particle contact condition so that the continuous measurement of shear wave velocity can reflect any small change in particle contacts (i.e., debonding of $CaCO_3$ at contacts). The input signal generated at the top cap was a square wave at 50 Hz generated by a waveform generator (Agilent 33220A), and the signal arrival at the bottom cap was captured by an oscilloscope (Agilent DSO5014) followed by signal amplification and band-pass filtering (Krohn-hite 3944, low-pass filter at f = 500 kHz, high-pass filter at f = 50 Hz).

The mixed reactive solutions of urea-$CaCl_2$ and urease filled the oedometric cell. Then, uniformly-graded Jumunjin sand (mean grain size D_{50} = 0.542 mm, minimum and maximum void ratios e_{min} = 0.6 and e_{max} = 0.897) was gently poured by pluviation. Two relative densities (30% and 70%) were achieved by tamping the soil specimens. $CaCO_3$ formation was allowed for 30 hours under a predetermined sitting pressure (σ'_{sit}) prior to the stress-induced debonding test.

In order to observe the effects of the loading sequences and sample conditions on the stiffness degradation, four sets of experiments were planned as schematically illustrated in Fig. 3b (loading steps represented by blue solid lines and unloading steps by red broken lines); Test A consisted of incremental loading starting at σ'_{sit} = 12 kPa followed by unloading for 0.5 M $CaCl_2$ and 1 M $CaCl_2$ solutions and for 30% and 70% relative density. Test B consisted of incremental loading starting at four σ'_{sit} values (12 kPa, 90 kPa, 180 kPa, and 532 kPa) followed by unloading and reloading. Test C consisted of decremental unloading starting at four σ'_{sit} values (90 kPa, 180 kPa, 532 kPa, and 1062 kPa) followed by loading and unloading. Test D consisted of repetitive loading and unloading cycles. For

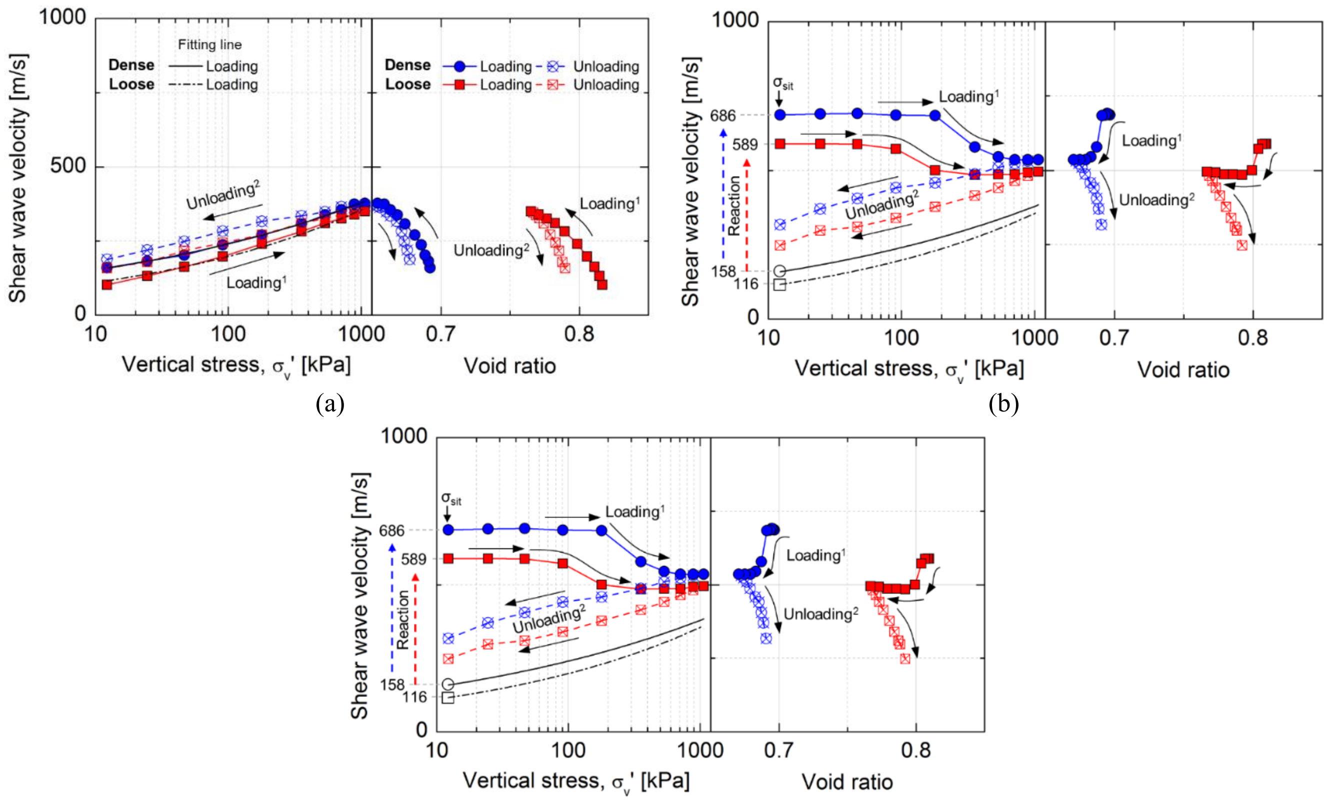

(a)

(b)

(c)

Fig. 4 Shear stiffness loss and re-gain and volume change during loading and unloading (Test A). (a) Non-treated sand specimen, (b) Treated with 0.5 M $CaCl_2$ and (c) treated with 1 M $CaCl_2$

Test A, two $CaCl_2$ concentrations (0.5 M and 1 M) and two initial relative density conditions (30% and 70%) were used (i.e., four individual tests). For Tests B, C, and D, samples were prepared with 0.5 M $CaCl_2$ solution and 70 % relative density. Each loading stage lasted 15 min under drainage conditions. The S-wave velocity was measured prior to applying the load in the next loading step by detecting the “zero after first bump” point as the first arrival (Lee and Santamarina 2005).

3. Responses to loading sequences

This section describes the gathered results of S-wave velocity evolution from Tests A to D and discusses the debonding mechanism at the particle scale.

3.1 Effect of concentration in EICP solution and relative density of soil (Test A)

For non-treated specimens, an increase in vertical stress increases the inter-particle contact area and improves the contact quality with decreasing void ratio; its manifestation is an increase of S-wave velocity (Yun and Santamarina 2005). By unloading, the shear wave velocity decreases and runs above its evolution during loading, and the void ratio slightly increases (Fig. 4a). Dense specimens exhibit higher V_s than loose specimens, and the computed values of the α-coefficient and β-exponent (α = 96, β = 0.19 for dense sand and α = 61, β = 0.25 for loose sand) for $V_s = \alpha \cdot \sigma'^{\beta}$ are well captured along the proposed tendency (Cha et al. 2014), implying the uncemented sand becomes stiffer under confinement.

When the sand is treated with 0.5 M $CaCl_2$ solution, the S-wave velocity significantly increases from 116 m/s to 589 m/s for loose specimens and from 158 m/s to 686 m/s for dense specimens, as a result of carbonate precipitation under a constant vertical stress of 12 kPa (Fig. 4b). Upon loading, the S-wave velocity remains constant up to σ'_v ~ 180 kPa for dense specimens and σ'_v ~ 46 kPa for loose specimens. Further increases in loading result in the rapid reduction in S-wave velocity while the void ratio gradually decreases. For the later loading steps up to ~ 1062 kPa, the S-wave velocity reaches a quasi-constant value of V_s = 536 m/s for dense and V_s = 495 m/s for loose specimens. Once the debonding takes place, V_s gradually decreases and the void ratio increases upon unloading, similar to the non-treated specimens. The reaction in 1.0 M $CaCl_2$ solution induces higher V_s values of 757 m/s and 880 m/s for loose and dense specimens (Fig. 4c). Upon loading, the stiffness loss is captured at ~ 90 kPa and 180 kPa, followed by the gradual reduction of V_s toward 602 m/s and 721 m/s for loose and dense specimens. The overall evolution of V_s and void ratio during loading and unloading is similar to the case of 0.5 M $CaCl_2$ solution. In addition, V_s values for treated specimens are always higher than those of non-treated specimens under the same vertical stress condition even after debonding occurs because of the existence of

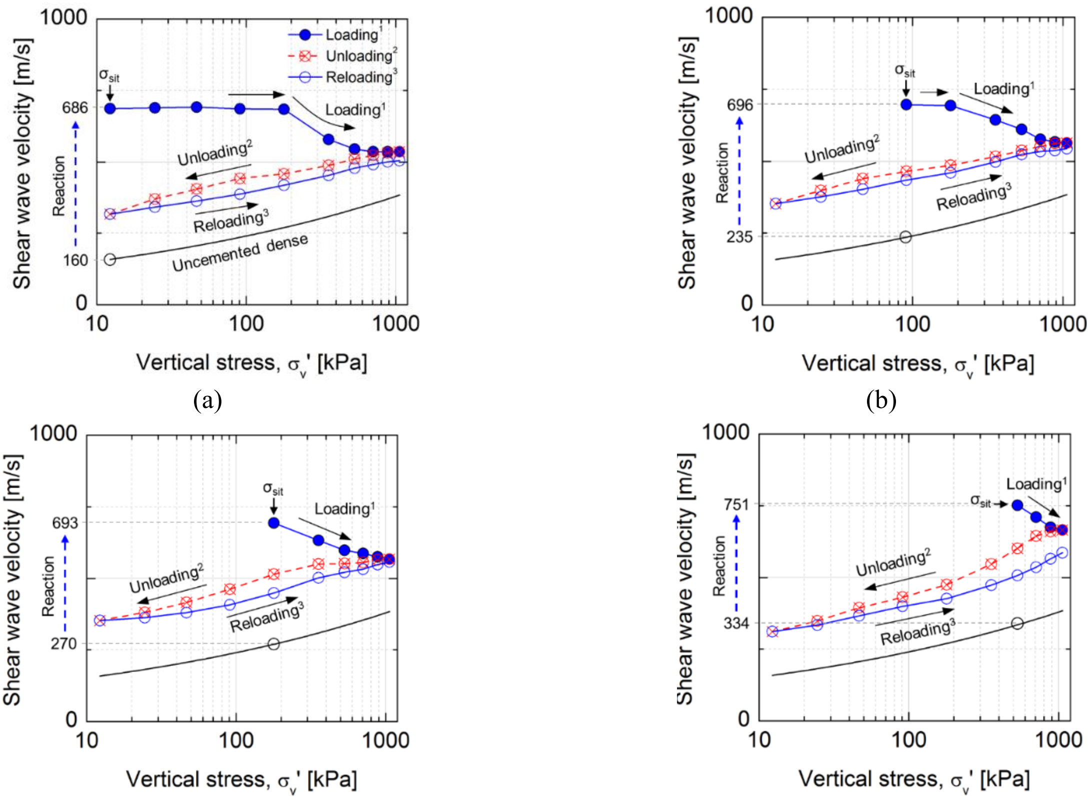

(a) (b)

(c) (d)

Fig. 5 Changes in shear wave velocity by initial compressional loading (Test B) of 0.5 M $CaCl_2$ and 70 % relative density specimens with sitting stress of (a) 12 kPa, (b) 90 kPa, (c) 180 kPa and (d) 532 kPa

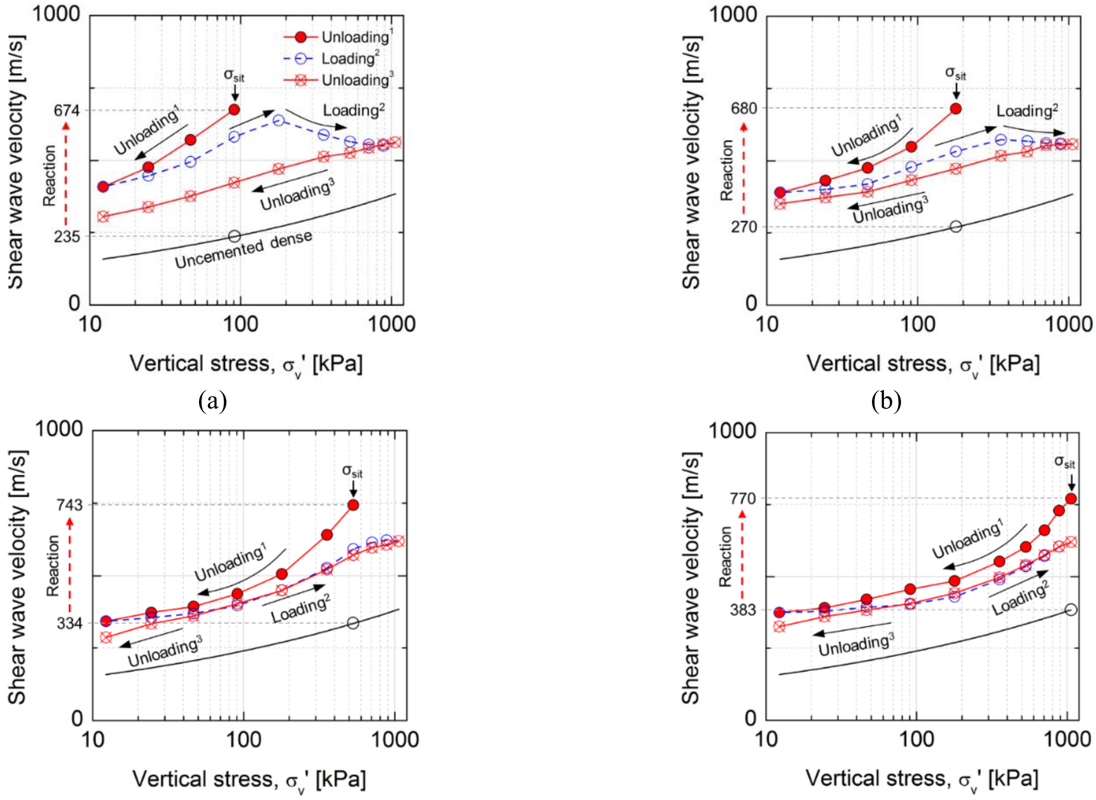

(a) (b)

(c) (d)

Fig. 6 Changes of shear wave velocity by initial stress relaxation (Test C) of 0.5 M $CaCl_2$ and 70 % relative density specimens. Sitting stresses are (a) 90 kPa, (b) 180 kPa, (c) 532 kPa and (d) 1062 kPa

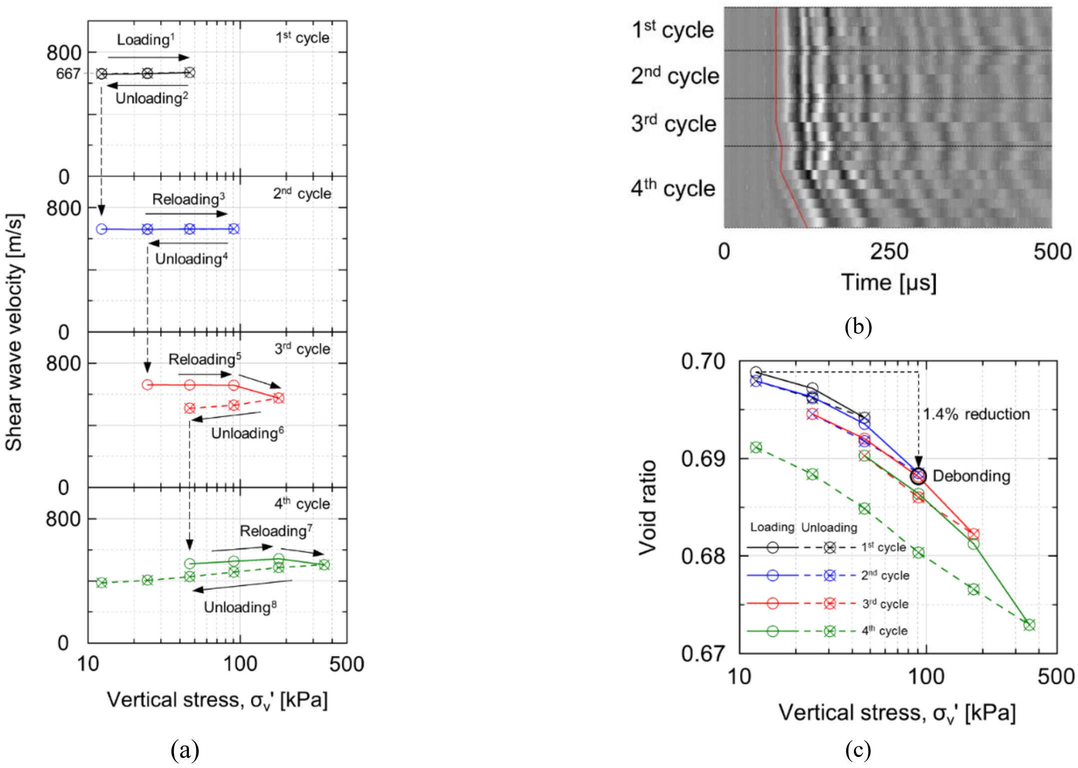

Fig. 7 Responses of shear wave and volume change for the specimen with 0.5 M $CaCl_2$ and 70 % relative density during loading-unloading cycles (Test D). (a) Shear wave velocity, (b) wave traces and (c) void ratio

$CaCO_3$ in pore space. Note that it is generally reported that compression in cemented sands causes both debonding of inter-particle contacts and volume collapse (Lee *et al.* 2010; Yun and Santamarina 2005), whereas the treated sand in this study does not experience the volumetric collapse because the sand particles are well packed prior to the carbonate precipitation. The vertical stress causing the stiffness loss is higher for dense specimens than for loose specimens, whereas its value is similar regardless of $CaCl_2$ concentration.

The mass fraction of $CaCO_3$/soil [g/g, %] measured from each specimen divided into four layers in vertical direction is that for 0.5M solution treated specimens, 1.33 ± 0.16 % for loose and 1.23 ± 0.13 % for dense are shown and for 1M solution treated specimens, 2.69 ± 0.22 % for looseand 2.36 ± 0.48 % for dense are shown. The error range of each specimen is from 8 % to 20 % that seems to be homogeneously distributed of $CaCO_3$ than the injection of solution that soil is strongly cemented near the injection part (Kavazanjian and Hamdan 2015).

3.2 Effect of sitting pressure (Test B)

As the sitting pressure increases, the specimen becomes highly compressed prior to the treatment; the $CaCO_3$ formation causes the increase in V_s. For initial sitting pressures of σ'_{sit} = 12 kPa and σ'_{sit} = 90 kPa (Figs. 5a and 5b), the initial V_s values of 686 m/s and 696 m/s are similar, indicating that the precipitated $CaCO_3$ mostly dominates the evolution of shear stiffness rather than the effect of confinement. Upon loading, the S-wave velocity remains constant until the vertical stress reaches σ'_v = 180 kPa; further loading results in V_s reduction. The S-wave velocity changes during unloading and reloading indicate that the precipitated $CaCO_3$ is no longer effective to the quality of inter-particle contact.

As shown in Figs. 5c and 5d, when the specimen is initially compressed by high sitting pressures (σ'_{sit} = 180 kPa and 532 kPa), the initial V_s values are 693 m/s and 751 m/s, which are slightly higher than for the previous cases, and the loading causes the immediate reduction of V_s. It is noted that the evolution of V_s during unloading and reloading is not remarkably different with the specimens made under four different σ'_{sit} values. This observation hints that initial compressional loading before cementation is sufficient to drive the extensive debonding, which is the major attribute of stiffness loss. In addition, it is worth noting that the debonding stress is σ'_v ~ 180 kPa for the specimen of 70 % relative density and treated with 0.5 M $CaCl_2$ solution, regardless of sitting pressure.

3.3 Unloading-Induced debonding (Test C)

The effect of stress relaxation on the bonding integrity at particle contact was investigated by unloading specimens treated at different sitting stresses. As shown in Fig. 6a, the specimen at σ'_{sit} = 90 kPa is initially unloaded and its shear wave velocity promptly decreases to 408 m/s at σ'_v = 12 kPa. During the loading stage, the shear wave velocity gently increases to 638 m/s (i.e., 95 % of the initial V_s = 674 m/s) until the vertical stress reaches σ'_v ~ 180 kPa, which happens to be the same as that in Figs. 4 and 5, over which the S-wave velocity decreases again. The second unloading leads to a gradual reduction in V_s, as commonly

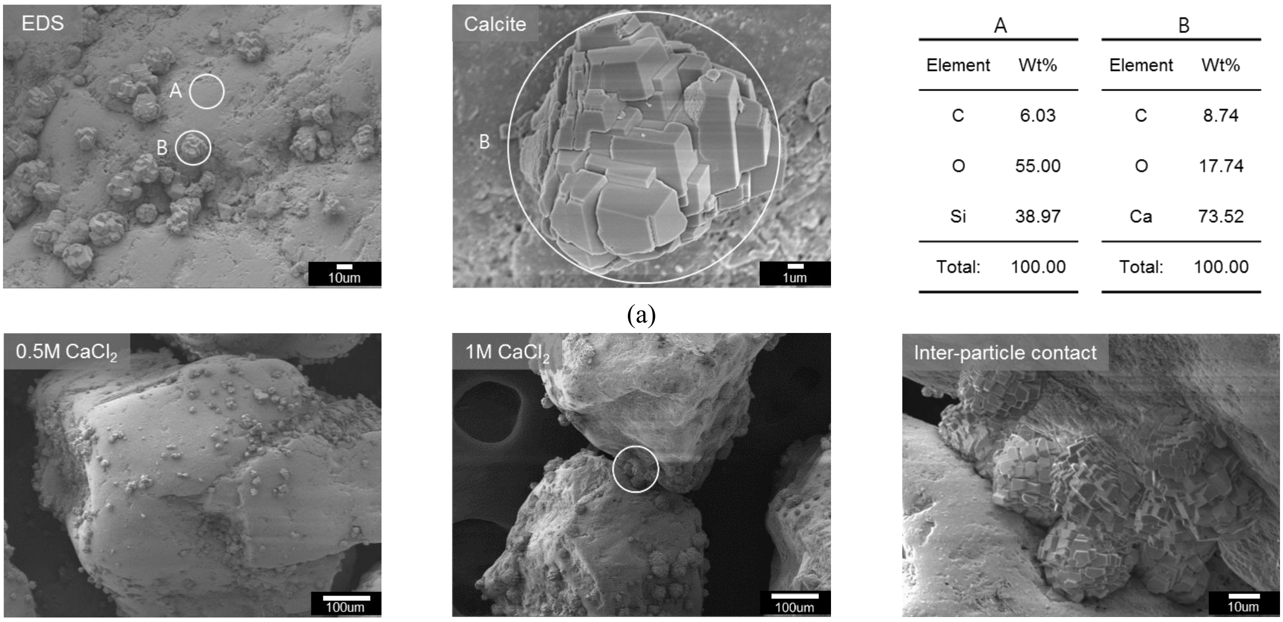

A		B	
Element	Wt%	Element	Wt%
C	6.03	C	8.74
O	55.00	O	17.74
Si	38.97	Ca	73.52
Total:	100.00	Total:	100.00

(a)

(b) (c) (d)

Fig. 8 Scanning electron microscopic (SEM) images of precipitated carbonates on sand grains. (a) Chemical compositions of A (silicate) and B ($CaCO_3$) analyzed by EDS, (b) 0.5 M $CaCl_2$ solution case, (c) 1.0 M $CaCl_2$ case and (d) Adjacent sand particles are bonded by $CaCO_3$

observed previously. Similarly, the specimen at σ'_{sit} = 180 kPa exhibits the prompt reduction of V_s by the first unloading, and the subsequent loading results in the increase of V_s up to σ'_v ~ 350 kPa, beyond which V_s decreases again (Fig. 6b). It therefore underlines that the stress relaxation by the first unloading should cause partial and incomplete debonding due to the tensional stress acting on the inter-particle contact, and the subsequent loading helps recover the shear stiffness followed by the secondary debonding. As shown in Figs. 6c and 6d, the stress relaxation from higher sitting stresses of σ'_{sit} = 532 kPa and 1062 kPa shows complete debonding and no secondary debonding during the loading step, presumably because the relief of highly compressed particles is sufficient to drive the complete debonding. Therefore, the bonding integrity can be deteriorated partially or completely by stress relaxation, depending on the initial sitting stress.

3.4 Response to repetitive loading and unloading (Test D)

The effect of repetitive loading and unloading cycles on the bonding integrity of cemented soil is discussed in this section. During the first and second cycles (σ'_v value from 12 kPa to 90 kPa), the S-wave velocity remains constant at ~ 667 m/s (Fig. 7a). However, it begins to decrease at σ'_v ~ 90 kPa which is lower than the previously observed debonding stress of 180 kPa. The repeated loading and unloading may weaken the intact bonding of $CaCO_3$ to particles, even though there is no noticeable change in V_s at σ'_v < 90 kPa. The specimens tend to sustain the subsequent loading at the fourth cycle without showing a stiffness loss up to ~ 180 kPa, beyond which a slight drop in V_s is observed. The time of first arrival, shown in red color in Fig. 7b, remains quasi-constant until the second cycle. There is a change in first arrival time during the third cycle when σ'_v = 90 kPa is applied. In the fourth cycle, the first arrival recedes, implying the debonding. Fig. 7c shows that the trend of void ratio as a function of vertical stress follows typical consolidation curves even in cemented status. When 90 kPa is applied in the third cycle, the void ratio is not significantly reduced, which was found previously as shown in Fig. 4b, and the reduction in voidratio is 1.4 %. Therefore, the repeated loading below a certain threshold stress may not cause the apparent loss of shear stiffness; the recurrent compression and tension can deteriorate the bonding quality between sand surface and precipitated $CaCO_3$ or between $CaCO_3$ particles.

4. Visual inspection of $CaCO_3$

The undisturbed and intact pieces of the samples treated with 0.5 M and 1 M $CaCl_2$ solutions were examined by SEM imaging (JEOL JSM-7610F) and 3D X-ray μ-CT imaging (SEC X-eye Micro CT). The size of 3D X-ray μ-CT imaging is 3.7 mm×3.7 mm×3.7 mm for 0.5 M $CaCl_2$ and 4 mm×4 mm×4 mm for 1 M $CaCl_2$ treated with dense specimens.

4.1 SEM analysis

The SEM image in Fig. 8a shows the chemical compositions of the rhombohedral structure of the nodule and sand particle surface by energy dispersive X-ray spectroscopy analysis. The chemical composition of A and B is silicate and $CaCO_3$ respectively, and the rhombohedral structure of $CaCO_3$ is calcite. Figs. 8b and 8c show the precipitated calcites existing in the form of small nodules

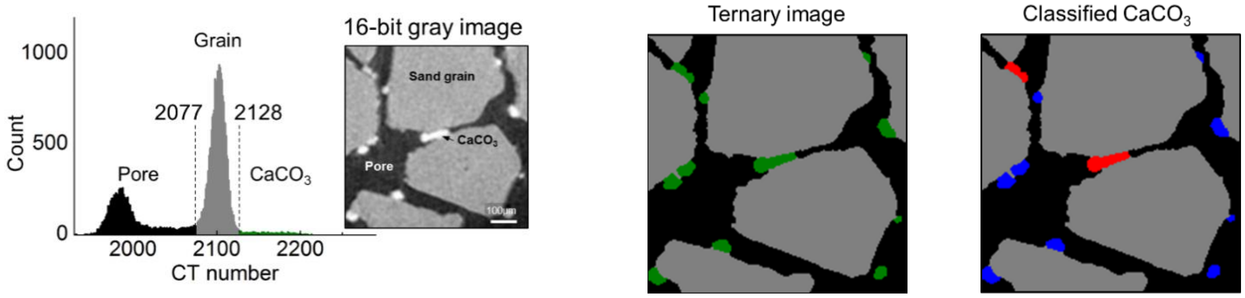

(a) (b) (c)

Fig. 9 (a) 16-bit gray scaled μ-CT image (e.g., dense sand treated with 1M $CaCl_2$). The white color indicates the carbonate nodules and the gray regions denote sand particles. Three components of pore, sand particles, and $CaCO_3$ are segmented by threshold values of 2077 and 2128 to make (b) the ternary image. (c) The carbonates formed on the grain surface (blue) and at the inter-particle contact (red) are classified by evaluating their contact condition

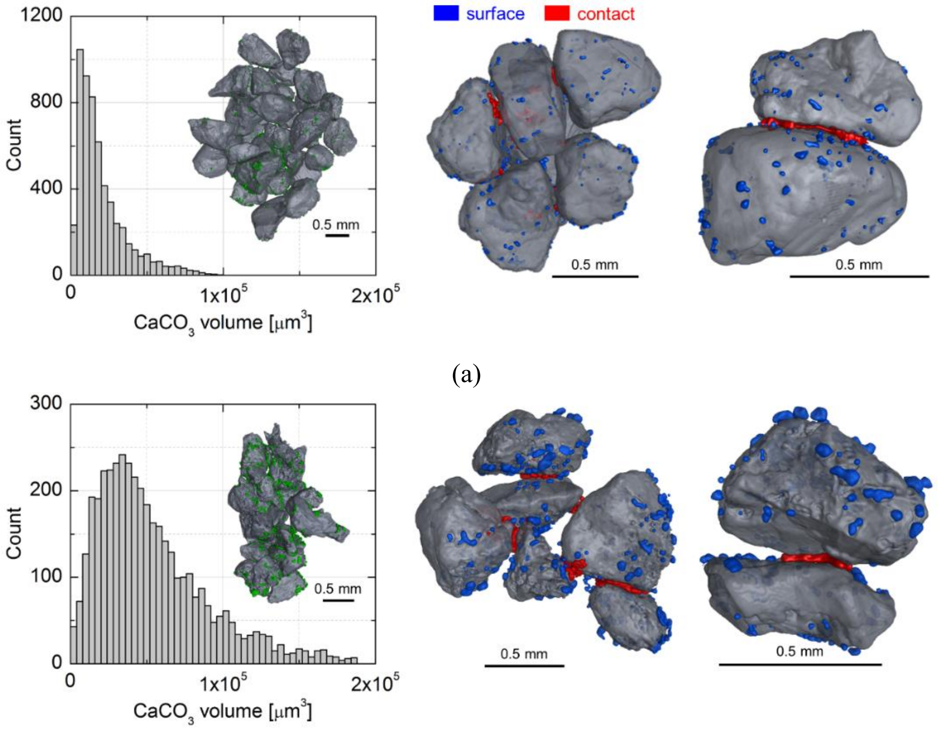

(a)

(b)

Fig. 10 Volume distribution of $CaCO_3$ nodules and their 3D spatial distribution of (a) 0.5 M $CaCl_2$ (mean volume: 20,126 μm^3) and (b) 1 M $CaCl_2$ (mean volume: 53,066 μm^3). $CaCO_3$ nodules formed at the inter-particle contact are illustrated in red-color while those on the grain surface are shown in blue-color

spreading over the sand surface. The calcite particle size is approximately 15 μm and 25 μm for 0.5 M and 1 M $CaCl_2$ specimens, respectively. The calcite nodules formed at the contact between sand particles can bind the adjacent sand particles, which is the primary reason for the V_s increase (Fig. 8d).

4.2 μ-CT analysis

μ-CT imaging was used to visualize the 3D spatial distribution of the precipitated calcites and estimate their contribution to shear stiffness evolution. Calcite particles (with density 2.71 g/cm^3) are represented by the white color, whereas the sand grains and pore space are displayed in bright gray and black in Fig. 9a, where the calcite nodules exist on sand grains or between two sand grains. The histogram of CT number exhibits three constituents outlined by threshold values so that the segmentation of calcite, sand grains, and pore is performed. Because there is no obvious hump between sand particles and calcite in the CT number histogram, a threshold value is determined when the visible calcite in the 16-bit grayscale image is apparently distinguished, and both sand particles and calcite nodules are segmented in Fig. 9b. With this segmented image, the calcite nodules precipitated in the sand surface and inter-particle contact are further classified by connected component analysis; each sand grain and calcite nodule is individually labeled, and we evaluate whether a given calcite nodule is in contact with a sand grain. If the calcite nodule is directly connected to more than two sand grains, it is classified as "contact calcite" (red color in Fig. 9c). On the other hand, it becomes "surface calcite" if a calcite nodule is in contact with a single sand grain (blue color in Fig. 9c). The 2D ternary images were reconstructed in 3D, and the mass fraction of calcite was computed with respect to the sands assuming that the densities of calcite and sand grains are 2.71 and 2.65 g/cm^3, respectively. The mass fraction was calculated by multiplying the density to the volume, which is the same as the pixel number.

For dense soil, the theoretical mass fraction of calcite is 0.013 and 0.026 for 0.5 M $CaCl_2$ and 1 M $CaCl_2$ solution, respectively. The total volume of sand in the 9.68 mm^3 and 8.58 mm^3 for 0.5M and 1M $CaCl_2$ and the total volume of calcite is 0.12 mm^3 and 0.22 mm^3 for 0.5 M $CaCl_2$ and 1 M $CaCl_2$, respectively. By multiplying the densities to volume of each material, the mass fraction obtained by the 3D images is 0.0124 and 0.0261 for 0.5 M $CaCl_2$ and 1 M $CaCl_2$ solution, which is well matched with the theoretically calculated mass fraction. The calculated fraction of inter-particle contact calcites to the total calcites is 12.06 % and 11.37 % for 0.5 M $CaCl_2$ and 1 M $CaCl_2$ solution. This means that approximately 11-12 % of the precipitated calcites directly contribute to the shear stiffness of the soil. A similar fraction of calcites formed at inter-particle contact was reported when the specimen was fully saturated with the solution; the fraction depends on the degree of saturation (Cheng and Cord-Ruwisch 2012).

Spatial distribution of calcite nodules in pore space and statistical distribution of the volume of the nodules are shown in Fig. 10. A relatively larger number of smaller-sized calcite nodules is formed with 0.5 M $CaCl_2$ solution, whereas fewer larger-sized calcite nodules are formed in the 1 M $CaCl_2$ solution. The mean volume of $CaCO_3$ nodules for 1 M $CaCl_2$ is 53,066 μm^3, which is 2.6 times that of 0.5 M $CaCl_2$ (20,126 μm^3). The larger size of the precipitated calcites is also shown at a higher concentration of urea-$CaCl_2$ solution in MICP- treated soil (Al Qabany *et al.* 2012). Because the 1 M $CaCl_2$ solution has a higher CO_3^{2-} concentration resulting from urea hydrolysis than in the 0.5 M $CaCl_2$, this result is well explained that the CO_3^{2-} is readily used for growing calcite crystal at high CO_3^{2-} concentrations (Somani *et al.* 2006).

5. Conclusions

This paper presents the experimental results of shear wave velocity and volume change in EICP-treated sand specimens subjected to various loading and unloading scenarios. The calcite formed in the sands was visualized by SEM and μ-CT to evaluate the morphological characteristics.

- The optimal recipe of EICP solution for the maximum reaction efficiency was identified as a molar ratio of urea to $CaCl_2$ of 1.5 with a urease concentration of 0.5 g/L and 0.9 g/L for 0.5 M $CaCl_2$ and 1 M $CaCl_2$ solutions, respectively.
- Subsequent compressional loading induces the stiffness loss at σ'_v = 180 kPa for dense specimens regardless of $CaCl_2$ solution concentration, whereas loose specimens exhibit lower debonding stress.
- When the specimen is compressed by an intermediate sitting pressure (e.g., less than σ'_{sit} = 180 kPa) prior to calcite precipitation, the unloading immediately induces the partial stiffness loss because of stress relaxation in compressed sand grains, and the subsequent loading drives the secondary debonding. However, for higher sitting pressure conditions of 532 kPa and 1062 kPa, the unloading causes complete debonding, and no partial debonding was observed during reloading stage.
- For the specimens subjected to repetitive loading and unloading cycles, the shear stiffness of EICP-treated sand remains constant and sustainable up to $\sigma'_v \sim 100$ kPa, despite the repeated loading and unloading, followed by stiffness loss on increased loading.
- The calcite nodules are precipitated in the form of a rhombohedral shape on the sand grain surface and at the contact between sand grains, and their size is more than twice for 1 M $CaCl_2$ solution than that for 0.5 M $CaCl_2$ solution. Image analysis shows that approximately 11–12 % of calcite nodules formed at the particle contact contribute to the changes in shear wave velocity.

Acknowledgments

This work was supported by the Land and Housing Institute (LHI) grant funded by the Korea Land and Housing Corporation, the National Research Foundation of Korea (NRF) grant funded by the Korea government (MSIT) (2016R1A2B4011292), and the research fund of the Korea Agency for Infrastructure Technology Advancement (KAIA) (18CTAP-C142849-01).

References

Al Qabany, A., Soga, K. and Santamarina, C. (2012), "Factors affecting efficiency of microbially induced calcite precipitation", *J. Geotech. Geoenviron. Eng.*, **138**(8), 992-1001. https://doi.org/10.1061/(ASCE)GT.1943-5606.0000666.

Al Qabany, A. and Soga, K. (2013), "Effect of chemical treatment used in MICP on engineering properties of cemented soils", *Géotechnique*, **63**(4), 331-339. http://dx.doi.org/10.1680/geot.SIP13.P.022.

Bahar, R., Benazzoug, M. and Kenai, S. (2004), "Performance of compacted cement-stabilised soil", *Cem. Concrete Compos.*, **26**(7), 811-820. https://doi.org/10.1016/j.cemconcomp.2004.01.003.

Burbank, M.B., Weaver, T.J., Williams, B.C. and Crawford, R.L. (2012), "Urease activity of ureolytic bacteria isolated from six soils in which calcite was precipitated by indigenous bacteria", *Geomicrobiol. J.*, **29**(4), 389-395. https://doi.org/10.1080/01490451.2011.575913.

Cha, M., Santamarina, J.C., Kim, H.S. and Cho, G.C. (2014), "Small-strain stiffness, shear-wave velocity, and soil compressibility", *J. Geotech. Geoenviron. Eng.*, **140**(10), 06014011. https://doi.org/10.1061/(ASCE)GT.1943-5606.0001157.

Cheng, L. and Cord-Ruwisch, R. (2012), "In situ soil cementation with ureolytic bacteria by surface percolation", *Ecol. Eng.*, **42**, 64-72. https://doi.org/10.1016/j.ecoleng.2012.01.013.

Chu, J., Ivanov, V., Naeimi, M., Stabnikov, V. and Liu, H.L. (2014), "Optimization of calcium-based bioclogging and biocementation of sand", *Acta Geotech*., **9**(2), 277-285. https://doi.org/10.1007/s11440-013-0278-8.

Consoli, N.C., Prietto, P.D.M. and Ulbrich, L.A. (1998), "Influence of fiber and cement addition on behavior of sandy soil", *J. Geotech. Geoenviron. Eng*., **124**(12), 1211-1214. https://doi.org/10.1061/(ASCE)1090-0241(1998)124:12(1211).

Cui, M.J., Zheng, J.J., Zhang, R.J., Lai, H.J. and Zhang, J. (2017), "Influence of cementation level on the strength behaviour of bio-cemented sand", *Acta Geotech*., **12**(5), 971-986. https://doi.org/10.1007/s11440-017-0574-9.

Cuthbert, M.O., Riley, M.S., Handley-Sidhu, S., Renshaw, J.C., Tobler, D.J., Phoenix, V.R. and Mackay, R. (2012), "Controls on the rate of ureolysis and the morphology of carbonate precipitated by S. Pasteurii biofilms and limits due to bacterial encapsulation", *Ecol. Eng*., **41**, 32-40. https://doi.org/10.1016/j.ecoleng.2012.01.008.

De Muynck, W., De Belie, N. and Verstraete, W. (2010), "Microbial carbonate precipitation in construction materials: A review", *Ecol. Eng*., **36**(2), 118-136. https://doi.org/10.1016/j.ecoleng.2009.02.006.

DeJong, J.T., Fritzges, M.B. and Nüsslein, K. (2006), "Microbially induced cementation to control sand response to undrained shear", *J. Geotech. Geoenviron. Eng.*, **132**(11), 1381-1392. https://doi.org/10.1061/(ASCE)1090-0241(2006)132:11(1381).

Fernandez, A.L. and Santamarina, J.C. (2001), "Effect of cementation on the small-strain parameters of sands", *Can. Geotech. J*., **38**(1), 191-199. https://doi.org/10.1139/t00-081.

Hamdan, N.M. (2015), "Applications of enzyme induced carbonate precipitation (EICP) for soil improvement", Ph.D. Dissertation, Arizona State University, Tempe, Arizona, U.S.A.

Huang, J.T. and Airey, D.W. (1998), "Properties of artificially cemented carbonate sand", *J. Geotech. Geoenviron. Eng*., **124**(6), 492-499. https://doi.org/10.1061/(ASCE)1090-0241(1998)124:6(492).

Ismail, M.A., Joer, H.A., Sim, W.H. and Randolph, M.F. (2002), "Effect of cement type on shear behavior of cemented calcareous soil", *J. Geotech. Geoenviron. Eng*., **128**(6), 520-529. https://doi.org/10.1061/(ASCE)1090-0241(2002)128:6(520).

Jiang, N.J., Soga, K. and Kuo, M. (2017), "Microbially induced carbonate precipitation for seepage-induced internal erosion control in sand–clay mixtures", *J. Geotech. Geoenviron. Eng*., **143**(3), 04016100. https://doi.org/10.1061/(ASCE)GT.1943-5606.0001559.

Kaniraj, S.R. and Havanagi, V.G. (2001), "Behavior of cement-stabilized fiber-reinforced fly ash-soil mixture", *J. Geotech. Geoenviron. Eng*., **127**(7), 574-584. https://doi.org/10.1061/(ASCE)1090-0241(2001)127:7(574).

Kavazanjian, E. and Hamdan, N. (2015), "Enzyme induced carbonate precipitation (EICP) columns for ground improvement", *Proceedings of the International Foundations Congress and Equipment Expo 2015*, San Antonio, Texas, U.S.A., March.

Kim, Y.M., Kwon, T.H. and Kim, S. (2017), "Measuring elastic modulus of bacterial biofilms in a liquid phase using atomic force microscopy", *Geomech. Eng*., **12**(5), 863-870. https://doi.org/10.12989/gae.2017.12.5.863.

Lee, C., Truong, Q.H. and Lee, J.S. (2010), "Cementation and bond degradation of rubber–sand mixtures", *Can. Geotech. J*., **47**(7), 763-774. https://doi.org/10.1139/T09-139.

Lee, J.S. and Santamarina, J.C. (2005), "Bender elements: performance and signal interpretation", *J. Geotech. Geoenviron. Eng*., **131**(9), 1063-1070. https://doi.org/10.1061/(ASCE)1090-0241(2005)131:9(1063).

Lin, H., Suleiman, M.T., Brown, D.G. and Kavazanjian, E. (2016), "Mechanical behavior of sands treated by microbially induced carbonate precipitation", *J. Geotech. Geoenviron. Eng*., **142**(2), 04015066. https://doi.org/10.1061/(ASCE)GT.1943-5606.0001383.

Mahawish, A., Bouazza, A. and Gates, W.P. (2018), "Effect of particle size distribution on the bio-cementation of coarse aggregates", *Acta Geotech*., **13**(4), 1019-1025. https://doi.org/10.1007/s11440-017-0604-7

Mitchell, J.K. and Santamarina, J.C. (2005), "Biological considerations in geotechnical engineering", *J. Geotech. Geoenviron. Eng*., **131**(10), 1222-1233. https://doi.org/10.1061/(ASCE)1090-0241(2005)131:10(1222).

Montoya, B.M., DeJong, J.T. and Boulanger, R.W. (2013), "Dynamic response of liquefiable sand improved by microbial-induced calcite precipitation", *Géotechnique*, **63**(4), 302-312. http://dx.doi.org/10.1680/geot.SIP13.P.019.

O'Rourke, T.D. and Crespo, E. (1988), "Geotechnical properties of cemented volcanic soil", *J. Geotech. Eng*., **114**(10), 1126-1147. https://doi.org/10.1061/(ASCE)0733-9410(1988)114:10(1126)/

Rios, S., Viana da Fonseca, A. and Baudet, B.A. (2014), "On the shearing behaviour of an artificially cemented soil", *Acta Geotech*., **9**(2), 215-226. https://doi.org/10.1007/s11440-013-0242-7.

Saxena, S.K., Reddy, K.R. and Avramidis, A.S. (1988), "Liquefaction resistance of artificially cemented sand", *J. Geotech. Eng*., **114**(12), 1395-1413. https://doi.org/10.1061/(ASCE)0733-9410(1988)114:12(1395).

Somani, R.S., Patel, K.S., Mehta, A.R. and Jasra, R.V. (2006), "Examination of the polymorphs and particle size of calcium carbonate precipitated using still effluent (i.e., CaCl2+ NaCl solution) of soda ash manufacturing process", *Ind. Eng. Chem. Res*., **45**(15), 5223-5230. https://doi.org/10.1021/ie0513447.

van Paassen, L.A., Ghose, R., van der Linden, T.J.M., van der Star, W.R.L. and van Loosdrecht, M.C.M. (2010), "uantifying biomediated ground improvement by ureolysis: large-scale biogrout experiment", *J. Geotech. Geoenviron. Eng*., **136**(12), 1721-1728. https://doi.org/10.1061/(ASCE)GT.1943-5606.0000382.

Yasuhara, H., Neupane, D., Hayashi, K. and Okamura, M. (2012), "Experiments and predictions of physical properties of sand cemented by enzymatically-induced carbonate precipitation", *Soils Found*., **52**(3), 539-549. https://doi.org/10.1016/j.sandf.2012.05.011.

Yun, T.S. and Santamarina, J.C. (2005), "Decementation, softening, and collapse: Changes in small-strain shear stiffness in k0 loading", *J. Geotech. Geoenviron. Eng*., **131**(3), 350-358. https://doi.org/10.1061/(ASCE)1090-0241(2005)131:3(350).

GC